On the kinetics of the methanation of carbon dioxide on coprecipitated NiAl(O)$_x$

Franz Koschany [a,b,1], David Schlereth [a,b,1], Olaf Hinrichsen [a,b,*]

[a] Technische Universität München, Department of Chemistry, Lichtenbergstraße 4, D-85748 Garching b. München, Germany
[b] Technische Universität München, Catalysis Research Center, Ernst-Otto-Fischer-Straße 1, D-85748 Garching b. München, Germany

ABSTRACT

A series of NiAl(O)$_x$ catalysts with varying Ni/Al ratio has been prepared by coprecipitation of the metal nitrate solutions with NaOH/Na$_2$CO$_3$ at constant pH. The samples have been analyzed by XRD, N$_2$ physisorption, temperature programmed reduction and H$_2$ chemisorption. For kinetic characterization, apparent activation energies and reaction orders are determined. The correlation of the catalytic acitivity and metallic surface area indicates a linear relationship. A data set comprising over 200 data points with varying gas composition, temperature and pressure has been recorded as a basis to develop a kinetic model that captures the intrinsic kinetics of the methanation of carbon dioxide under process relevant conditions. As rate equations power laws, power laws with inhibition, for instance by water, and Langmuir–Hinshelwood–Hougen–Watson (LHHW) approaches are evaluated. Modeling results emphasize that the kinetics at differential conversions and pure H$_2$/CO$_2$ feed markedly differ from the regime closer to equilibrium. Power laws with inhibition and adequate LHHW approaches are capable to reflect the kinetics over a wide range of conditions from differential conversion to thermodynamic equilibrium.

© 2015 Elsevier B.V. All rights reserved.

1. Introduction

The expected depletion and rising demand of conventional, easily exploitable fossil fuels as well as the intention to reduce carbon dioxide emissions, which is seen as a major driver of the greenhouse effect and climate change, are widely expected to dramatically change the future energy and fuel supply. In particular, wind and photovoltaic energy as well as biomass will increasingly supplement the energy mix. The European Union, for instance, set the aim to cut its greenhouse gas emissions to 80% below 1990 levels by the year of 2050 [1]. The transition to renewables will inter alia comprise two challenges: in contrast to conventional power plants, renewable energy will not be constantly available but will depend on weather, day and night, or season etc.. Furthermore, the generation of renewable energy might locally be preferred in remote areas. Consequently, there is a need to store energy when available, to provide it fast on demand and to transport it cheaply and efficiently. Also, one might think of converting renewable energy to transportable fuels for mobile applications that can make use of well-established combustion engines. The chemical storage by means of so-called chemical energy carriers and in particular of syn-

thetic natural gas (SNG) offers one possibility that might meet the mentioned requirements [2–5]. When available, renewable energy can be used to electrolyze water to hydrogen and oxygen. Hydrogen can then be converted with carbon dioxide separated for instance from off gas of fossil power plants, cement industry, biomass conversion or even from atmosphere to methane. Methane can easily be stored in the gas grid or gas reservoirs, transported via the gas grid and reconverted, using solely already existing infrastructure. The concept has also been transferred to the application as transport fuel [6].

The heart of the power-to-gas concept is the methanation process. The reaction of carbon dioxide with hydrogen to methane and water is a highly exothermic as well as under standard conditions exergonic reaction with volume contraction:

$$CO_2 + 4H_2 \rightleftharpoons CH_4 + 2H_2O$$
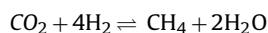
$$\Delta H_R^0 = -165 \text{ kJ/mol} \quad \Delta G_R^0 = -114 \text{ kJ/mol}$$

According to Le Chatelier's principle, low temperatures and high pressures shift the equilibrium to the product side. Quantitatively, a yield of methane of 95% with a selectivity close to 100% is obtained at 300 °C in thermodynamic equilibrium assuming a total pressure of 1 bar and stoichiometric feed gas composition of 80% hydrogen and 20% carbon dioxide. This corresponds to a methane content of 80% in the product gas after removal of water. The conversion of

carbon dioxide passes a minimum at 585 °C of 65%. Higher temperatures favor carbon monoxide over methane, which is formed via the endothermic reverse water–gas shift. The CO content at 1 bar is in the low ppm-range (<50 ppm) for temperatures below 300 °C. A detailed analysis of thermodynamic aspects of carbon dioxide methanation has been presented in ref. [7].

Though the heterogeneously catalyzed reaction of carbon dioxide with hydrogen to methane and water has been well known since beginning of the 20th century – it was discovered by Nobel laureate Paul Sabatier in the 1900s [8] –, kinetic models applicable for technical conditions are scarce. Nevertheless, they are strongly needed for reactor design and optimization and also for a qualified comparison of different catalyst systems. In view of economic feasibility we focused on Ni based systems though Rh [9–11], Ru [12–16] and Pd [17,18] have also been reported as catalytically active. Table 1 gives an overview of published models. First kinetic investigations have been presented in the 1950s. For instance, Dew et al. studied kinetics on a pelletized Ni kieselguhr catalyst [19]. As kinetics were measured on pelletized catalysts of about 3×3 mm size in an undiluted fixed-bed, one can, however, not exclude that they were biased by heat and mass transfer processes. Measurements were restricted to initial reaction rates, which were fitted by simple so-called "generalized rate equations". To the best of our knowledge, the first detailed mechanistic model for intrinsic kinetics for a Ni-based catalyst has been presented by Weatherbee and Bartholomew [20] for 3 wt.% Ni/SiO_2, however, at highly diluted gas composition. Accordingly, partial pressures of carbon dioxide (2.76–27.6 mbar) and hydrogen (27.6–138 mbar) are far away from a possible technical realization of a SNG process, where almost complete conversion to methane contents of above 95% in the dried product gas are desired, so that the product gas can directly be fed into the gas grid without further purification or separation steps. In this respect, elevated pressures will be necessary to shift the equilibrium accordingly. Relevant process patents mention pressures between 2 and 15 bar and reactor outlet temperatures as low as 250 °C [21].

Further progress concerning kinetics was accomplished by Kai et al. [27], who used both a differential and an integral reactor for kinetic studies at ambient pressure on an alumina supported Ni catalyst promoted by La_2O_3. By operating the integral reactor up to conversions of 90%, the influence of the products water and methane on the kinetics was accessible in greater detail than in previous studies. Kinetics were described by a Langmuir–Hinshelwood rate equation based on the mechanism proposed by Weatherbee and Bartholomew [20], but assuming the hydrogenation of carbon instead of CO dissociation as rate determining step. It was found that measured conversions at integral operation were smaller than predicted by rate equations based on experiments run in differential mode. This was attributed to the adsorption of products on the catalyst surface. As a consequence, the adsorption of water was accounted for in the Langmuir–Hinshelwood rate equation and an excellent fit of the data was obtained this way.

As part of the comprehensive kinetics of steam reforming, also experiments on the methanation of CO_2 were performed on a typical steam reforming 15 wt.% $Ni/MgAl_2O_4$ catalyst and used for parameter estimation for steam reforming and methanation kinetics by Xu and Froment [28]. Experimental conditions concerning the methanation experiments were temperatures between 300 and 400 °C and pressures between 3 and 8 bar, which are close to a technical implementation of CO_2 methanation.

Against the background of previously published kinetics, we present a kinetic model for a state-of-the-art catalyst system, which has recently been published and proven superior activity in comparison to other Ni based catalyst systems [29]. So far, investigations of intrinsic kinetics for the methanation of carbon dioxide were based on relatively low loaded systems as in case of Weatherbee and Bartholomew (3 wt.%) [20] or Kai et al. (17 wt.%) [27] or even on steam reforming catalysts as in case of Xu and Froment [28]. Furthermore, chosen conditions for kinetic experiments are relevant for technical operation intended to the production of SNG, i.e., elevated pressures and high hydrogen and carbon dioxide contents in the feed gas, in contrast to the studies by Weatherbee and Bartholomew [20] or Kai et al. [27]. Thereby, we measured not only both in differential and integral mode, but for the first time dosed methane and water already in the feed in order to capture their influence on the kinetics and apparent reaction orders in detail. In comparison to previous kinetic studies, we supply a characterization of the employed catalysts and relate to a series of catalysts with varying Ni content and specific Ni surfaces.

To summarize, the main objective of our paper is to derive a kinetic model, which is capable of reflecting intrinsic methanation kinetics for a state-of-the-art catalyst under industrially relevant conditions. In detail, we will first present and discuss characterization results comprising elementary analysis, powder X-ray diffraction (XRD), N_2 physisorption, temperature programmed reduction (TPR), and hydrogen chemisorption for a series of varying (1/5–5/1) Ni/Al molar ratio. We chose this relatively wide range in order to potentially study catalysts of varying precursor structure or varying physical properties like specific Ni surfaces or crystallite sizes. The catalytic activity of the systems will be compared and related to characterization results. For a selected catalyst different kinetic models comprising power laws, power laws with inhibition and Langmuir–Hinshelwood–Hougen–Watson (LHHW) approaches will be evaluated in order to assess the level of detail needed for reflection of kinetics from differential to almost complete conversion.

2. Experimental

2.1. Catalyst synthesis

The nickel-alumina precursors were prepared by coprecipitation at constant pH following the synthesis route described in ref. [29]. The purity of all used reagents was p.a., water was purified by a Millipore® water clearing rig, gas was purchased from Westfalen AG with a purity of 6.0 for H_2 and 5.0 for all other gases. For precipitation a double-walled glass vessel with a volume of 3 l was used, preloaded with 1 l H_2O, heated to 30 °C and stirred by a KPG stirrer with 250 min^{-1}. Additionally two flow breakers were inserted in the vessel to improve mixing. 120 ml of the mixture of the aqueous solutions of the metal nitrates (1 M $Ni(NO_3)_2 \cdot 6H_2O$, Merck® and 1 M $Al(NO_3)_3 \cdot 9H_2O$, Sigma–Aldrich®), were added by a medorex peristaltic pump with 8 ml min^{-1}. As precipitating agent a mixture of 0.5 M NaOH (Merck®) and 0.5 M Na_2CO_3 (Sigma–Aldrich®) was used. The Titrino Autotitrator 716DMS by Methrom® dosed the solution into the vessel to hold the pH constant at 9 ± 0.1 during the precipitation. The molar ratio of Ni/Al was varied between 5/1 and 1/5, denoted for instance as NiAl51 and NiAl15, respectively. For reason of comparison, two samples containing only Ni or only Al were precipitated in the same way. The product slurry was stirred and aged in the mother liquor for 18 h. After washing until pH was constant and drying at 80 °C overnight, the precursors were calcined at 450 °C for 6 h under synthetic air flow (heating rate 5 °C min^{-1}). For reduction the catalyst was heated up to 485 °C by 2 °C min^{-1} in a 5 vol.% H_2 in Ar flow and kept there for 11 h.

2.2. Catalyst characterization

For powder X-ray diffraction analysis a Philips X'pert with Cu-K_α radiation and a monochromator was used. The diffractogram resulted from a scanning in the range between $2\theta = 5$–70° step-

Table 1
Overview of kinetic models presented in literature.

Catalyst (Ni wt.%)	T [°C]	p_{max} [bar]	Rate equation	Ref.
Ni/SiO$_2$ (60)	260–400	1	$r_{CH_4} = \dfrac{k\left(p_{CO_2}p^2_{H_2} - p_{CH_4}p^2_{H_2O}/K_{eq}p^2_{H_2}\right)}{\left(1 + K_{H_2}p^{0.5}_{H_2} + K_{CO_2}p_{CO_2}\right)^5}$ $r_{CH_4} = \dfrac{k\left(p_{CO_2}p^4_{H_2} - p_{CH_4}p^2_{H_2O}/K_{eq}\right)}{\left(1 + K_{H_2}p^{0.5}_{H_2} + K_{CO_2}p_{CO_2}\right)^9}$	[22]
Ni/SiO$_2$ (60)	280–400	30	$r_{CH_4} = \dfrac{kp_{CO_2}p^4_{H_2}}{\left(1 + K_{H_2}p_{H_2} + K_{CO_2}p_{CO_2}\right)^5}$	[19]
Ni/Cr$_2$O$_3$ (62)	160–180	1	$r_{CH_4} = kp^{0.5}_{CO_2}$	[23]
Ni/Al$_2$O$_3$ (28)	200–230	1	$r_{CH_4} = \dfrac{kp_{CO_2}}{1 + A_{CO_2}p_{CO_2}}$	[24]
Ni/SiO$_2$ (3)	227–327	0.16	$r_{CH_4} = \dfrac{kp^{0.5}_{CO_2}p^{0.5}_{H_2}}{\left(1 + K_1p^{0.5}_{CO_2}p^{0.5}_{H_2} + K_2p^{0.5}_{CO_2}/p^{0.5}_{H_2} + K_3p_{CO}\right)^2}$	[20]
Ni/SiO$_2$ (58)	275–320	17	$r_{CH_4} = kp^{0.66}_{CO_2}p^{0.21}_{H_2}$ $r_{CH_4} = \dfrac{kp_{CO_2}p_{H_2}}{\left(1 + K_{H_2}p_{H_2} + K_{CO_2}p_{CO_2}\right)}$	[25]
Ni	250–350	n.a.	$r_{CH_4} = \dfrac{kp_{H_2}p^{1/3}_{CO_2}}{1 + K_{CO_2}p_{CO_2} + K_{H_2}p_{H_2} + K_{H_2O}p_{H_2O}}$	[26]
Ni/La$_2$O$_3$/Al$_2$O$_3$ (17)	240–320	1	$r_{CH_4} = \dfrac{kp^{1/2}_{H_2}p^{1/3}_{CO_2}}{\left(1 + K_{H_2}p^{1/2}_{H_2} + K_{CO_2}p^{1/2}_{CO_2} + K_{H_2O}p_{H_2O}\right)^2}$	[27]
Ni/MgAl$_2$O$_4$ (15)	300–400	10	$r_1 = \dfrac{k_1}{p^{2.5}_{H_2}} \dfrac{p_{H_2O}p_{CH_4} - \frac{p^3_{H_2}p_{CO}}{K_1}}{\left(1 + K_{CO}p_{CO} + K_{H_2}p_{H_2} + K_{CH_4}p_{CH_4} + K_{H_2O}p_{H_2O}/p_{H_2}\right)^2}$ $r_2 = \dfrac{k_2}{p_{H_2}} \dfrac{p_{H_2O}p_{CO} - \frac{p_{H_2}p_{CO_2}}{K_2}}{\left(1 + K_{CO}p_{CO} + K_{H_2}p_{H_2} + K_{CH_4}p_{CH_4} + K_{H_2O}p_{H_2O}/p_{H_2}\right)^2}$ $r_3 = \dfrac{k_3}{p^{3.5}_{H_2}} \dfrac{p^2_{H_2O}p_{CH_4} - \frac{p^4_{H_2}p_{CO_2}}{K_3}}{\left(1 + K_{CO}p_{CO} + K_{H_2}p_{H_2} + K_{CH_4}p_{CH_4} + K_{H_2O}p_{H_2O}/p_{H_2}\right)^2}$	[28]

wise with 0.017° step^{-1} and recording rate of 95.6 steps min^{-1}. The surface area of the calcined precursor was calculated, using BET analysis in the p/p_0 range between 0.05 and 0.30 of the N$_2$ adsorption isotherms at −196 °C. It was measured by a NOVA 4000e from Quantachrome. Prior to measurement the samples were heated under vacuum up to 120 °C for 3 h. H$_2$ chemisorption was performed with an Autosorb-1 (Quantachrome) at 35 °C after activation as mentioned above (5% H$_2$ in N$_2$, heating rate 2 °C min^{-1}–485 °C). The specific nickel surface area was calculated following the extrapolation theory, details are given in the Appendix A. Catalyst composition was determined by elementary analysis using an AA280FS atom absorption spectrometer from VARIAN. For thermogravimetric analysis a Netsch STA409 cell equipped with an Omnistar QMS (Pfeiffer GSD 301 O2) was used. TPR was conducted with 5% H$_2$ in Ar with a total flow of 60 sccm (heating rate 4 °C min^{-1}–500 °C, holding for 390 min).

2.3. Experimental setup

For the kinetic measurements a two line setup was employed. The main parts consist of gas mixing and dosing, the reactor section and the analysis section. All gases were provided by Westfalen AG, for the measurements H$_2$ (6.0), CO$_2$ (5.0), Ar (5.0) and CH$_4$ (5.0) were used. The gases were dosed by mass flow controllers (MFC), before entering the reaction zone. Water can be added by a vaporizer. To prevent condensing, all tubing is heated. The reaction zone consists of two reactor lines, which can independently be heated up to 600 °C and pressurized up to 20 bar. The catalyst bed is fixed with silica wool plugs in the isothermal zone of a glass lined steel tubing with an inner diameter of 4 mm. The reactor temperature is measured at the end of the catalytic bed. Leaving the reactor, the product gas is diluted with Argon, to prevent water condensation in the analytics. The latter includes a Pfeiffer Vacuum

Thermostar mass spectrometer (MS) for supervising transient measurements, an Emerson MTL-4 online IR process gas analyzer (PGA) and a PerkinElmer gas chromatograph (GC) which is equipped with two FID detectors for byproduct analysis. The PGA detects the concentration of CO, CO$_2$, CH$_4$, H$_2$, and H$_2$O in the gas stream online and the results are used for the quantitative analysis. To ensure steady conditions and reproducibility, the catalyst is hold under the particular conditions for 45 min and the data point is averaged over the last three minutes

2.4. Kinetic measurements

The kinetic data pool was recorded with 25 mg catalyst in the temperature range from 250 to 340 °C and 75 mg between 180 and 240 °C. The catalyst was diluted with purified SiC in the catalyst-to-SiC ratio of 1/9 using the same particle sizes of 0.15–0.20 mm. It has been checked that the purified SiC is not catalytically active. For reduction, the catalyst was heated with 2 °C min^{-1} to 485 °C in a flow of H$_2$/Ar = 5/95, the temperature kept for 11 h and the hydrogen consumption monitored in the MS. This was followed by an aging period at 380 °C and 7 bar$_{abs}$ for 300 h. The flow rate was 120 Nl h^{-1} g$_{cat}^{-1}$ and the feed contains H$_2$/CO$_2$/CH$_4$/H$_2$O/Ar in the ratio of 4/1/1.25/2.5/1.25. A feed mixture containing water and methane during the aging period has proven advantageous to prevent deactivation during the parameter study concerning an activity loss, when the catalyst has first contact with water. In the subsequent measurements on the aged catalyst, a variation of the process parameters corresponding to Table 2 was conducted. During parameter variation possible deactivation of the catalyst was monitored by reference point measurements at least every 24 h. It has been checked that all data points of the parameter variation fulfill the Mears, Anderson and Weisz-Prater criteria so that intra-particle and external heat and mass transfer limitations are not

Table 2
Variation of process parameters during the kinetic measurements.

Temperature [°C]	Feed		Flow [Nl h⁻¹ g⁻¹_cat]	Pressure_abs [bar]	Mass_Cat [mg]
	H_2/CO_2	CH_4/H_2O			
180–240	0.25–4	-/-	36, 48	1–15	75
250–340	0.25–8	-/- or 1/2	120,150,180	1–9	25

expected to affect the kinetic measurements (see Appendix A.1 for details).

3. Methodology

3.1. Kinetic rate equations

3.1.1. Power law rate equations

Different kinetic models will be evaluated and compared. The simplest model studied is a power law (PL) solely considering the reaction orders of hydrogen and carbon dioxide:

$$r = k \cdot p_{H_2}^{n_{H_2}} p_{CO_2}^{n_{CO_2}} \left(1 - \frac{p_{CH_4} p_{H_2O}^2}{p_{H_2}^4 p_{CO_2} K_{eq}} \right)$$

The equilibrium constant K_{eq} is calculated based on the species' enthalpies and entropies according to the Shomate equation and data provided by NIST Chemistry WebBook. Alternatively, the equilibrium constant could also be approximated by the empirical formula

$$K_{eq} = 137 \cdot T^{-3.998} \exp \left(\frac{158.7 kJ/mol}{RT} \right)$$

[30].

The model PL will also be used to evaluate the reaction orders of carbon dioxide and hydrogen in dependence of feed composition. If an inhibiting influence of water is considered via a power term, the model is extended to five parameters (PL-H2O):

$$r = k \cdot \frac{p_{H_2}^{n_{H_2}} p_{CO_2}^{n_{CO_2}}}{p_{H_2O}^{n_{H_2O}}} \left(1 - \frac{p_{CH_4} p_{H_2O}^2}{p_{H_2}^4 p_{CO_2} K_{eq}} \right)$$

Inhibition by adsorbed water (PL–WI) or adsorbed hydroxyl (PL–HI) can empirically be treated via the following equations comprising six parameters.

$$r = k \cdot \frac{p_{H_2}^{n_{H_2}} p_{CO_2}^{n_{CO_2}}}{1 + K_{H_2O} p_{H_2O}} \left(1 - \frac{p_{CH_4} p_{H_2O}^2}{p_{H_2}^4 p_{CO_2} K_{eq}} \right) \text{ and}$$

$$r = k \cdot \frac{p_{H_2}^{n_{H_2}} p_{CO_2}^{n_{CO_2}}}{1 + K_{OH} \frac{p_{H_2O}}{p_{H_2}^{1/2}}} \left(1 - \frac{p_{CH_4} p_{H_2O}^2}{p_{H_2}^4 p_{CO_2} K_{eq}} \right)$$

All rate and adsorption constants are treated as Arrhenius-type, all adsorption constants as van't Hoff-type:

$$K_x = K_{x,0} \cdot \exp \left(-\frac{E_A}{RT} \right) \text{ and } k_x = k_{x,0} \cdot \exp \left(-\frac{\Delta H_X}{RT} \right)$$

They are parameterized in order to minimize the correlation between preexponential factor and activation energy or adsorption enthalpy, respectively, during parameter estimation:

$$k = k_{0,ref} \cdot \exp \left(\frac{E_A}{R} \left(\frac{1}{T_{ref}} - \frac{1}{T} \right) \right) \text{ and}$$

$$K_x = K_{x,0,ref} \cdot \exp \left(\frac{\Delta H_X}{R} \left(\frac{1}{T_{ref}} - \frac{1}{T} \right) \right)$$

Table 3
Mechanisms a (left) and b (right) for derivation of LHHW rate equations.

1: CO_2	+ 2*	⇌	CO^*	+ O^*	1: CO_2	+ 2*	⇌ CO^*	+ O^*
2: H_2	+ 2*	⇌	2 H^*	+	2: H_2	+ 2*	⇌ 2 H^*	+
3: CO^*	+ *	⇌	C^*	+ O^*	3: CO^*	+ H^*	⇌ CHO^*	+ *
4: C^*	+ H^*	⇌	CH^*	+ *	4: CHO^*	+ *	⇌ CH^*	+ O^*
5: O^*	+ H^*	⇌	OH^*	+ *	5: CH^*	+ 3H^*	⇌ CH_4^*	+ 3*
6: OH^*	+ H^*	⇌	H_2O^*	+ *	6: CH_4^*		⇌ CH_4	+ *
7: H_2O^*		⇌	H_2O	+ *	7: O^*	+ H^*	⇌ OH^*	+ *
8: CH^*	+ 3H^*	⇌	CH_4^*	+ 3*	8: OH^*	+ H^*	⇌ H_2O^*	+ *
9: CH_4^*		⇌	CH_4	+ *	9: H_2O^*		⇌ H_2O	+ *

3.1.2. LHHW rate equations

LHHW-type rate equations are derived analogously to the methodology of Weatherbee and Bartholomew [20] that recently was also adopted for the methanation of carbon monoxide by Kopyscinski et al. [31,32]. The first mechanism assumed (Table 3 left) considers the cleavage of carbon-oxygen bonds first and subsequent hydrogenation of carbon and carbenes to methane as well as hydrogenation of adsorbed oxygen to water. Hydrogen, carbon dioxide and methane are assumed to adsorb dissociatively. This mechanism is the same as assumed by Weatherbee and Bartholomew. It has been formulated in analogy to CO methanation based both on the observation that CO_2 adsorbs dissociatively and a TPSR study by Falconer and Zagli [33]. Therein, carbon dioxide was preadsorbed at elevated temperatures, subsequently cooled and hydrogen was fed. At room temperature, water was detected and the following signal was the same as found for CO methanation. For sake of comparison, a second mechanism is formulated in analogy to a so-called hydrogen assisted pathway in CO methanation where first hydrogen reacts with CO to carbon–hydroxyl COH or formyl HCO, respectively, before carbon oxygen bond cleavage [30,32,34,35]. In Table 3, a mechanism is exemplarily formulated with adsorbed carbon monoxide, which results from the first carbon–oxygen bond cleavage of carbon dioxide, being first hydrogenated to a formyl species before the second C—O bond cleavage to a CH-species. Such a mechanism has for example also been formulated by Blaylock et al. in a DFT study about possible mechanisms for steam reforming [36]. The mechanism in Table 3 comprising a formyl species is by no means unique. A formyl species has for example also been proposed by Aparicio in a microkinetic model for reforming and methanation [30]. There, formyl is assumed to be formed by cleavage of formate HCOO, resulting from the reaction of adsorbed carbon dioxide and hydrogen. Of course, further mechanisms could have been formulated comprising COH or HCOO, respectively (cf. [37–40]). However, the variability introduced by this two mechanisms proved sufficient (see also the discussion in Section 4.3 about inferring the mechanism). Based on the two formulated mechanisms, over 20 rate equations are derived by varying the rate determining step and assuming further irreversible steps. The rate equation assuming step 3 of mechanism b as rate determining step and step 8 in addition as irreversible is derived for clarity in the Appendix. As most abundant surface intermediate hydrogen, the species present in the RDS and water or hydroxyl are considered.

The LHHW models are discriminated using Bartlett's X^2 test where the variances between experiments and all models are tested upon equality. If this hypothesis is rejected, the model with

Table 4
Characterization results.

	Ni	NiAl51	NiAl31	NiAl11	NiAl13	NiAl15	Al
elementary analysis n_{Ni}/n_{Al} [–] stoichiometric formula[a]	–	5.5 $NiAl_{0.18}(CO_3)_{0.2}(OH)_{2.1}$	3.4 $NiAl_{0.29}(CO_3)_{0.19}(OH)_{2.5}$	1.2 $NiAl_{0.86}(CO_3)_{0.29}(OH)_4$	0.37 $NiAl_{2.7}(CO_3)_{0.45}(OH)_{9.2}$	0.23 $NiAl_{4.4}(CO_3)_{0.55}(OH)_{14.1}$	–
BET surface area[b] $[m^2 g^{-1}_{cat}]$	26.1	128	149	235	229	229	223
specific Ni surface area[c] $[m^2 g^{-1}_{cat}]$	1.2	36.1	31.6	21.3	9.2	4.4	0
Ni dispersion[c] [%]	0.17	6.3	5.9	6.1	4.6	3.2	–
average crystallite size[c] [nm]	583	16.1	17.1	16.6	22.0	32.1	–
WTY[d] $[\mu mol\, s^{-1}\, g^{-1}_{cat}]$ (TOS = 0 h)	2.4	108	92.6	81.0	29.9	20.3	–

[a] Precursor composition after drying at 80 °C based on elementary analysis of C, Ni, Al.
[b] Calcined samples.
[c] Following extrapolation theory.
[d] $T = 250$ °C, $p = 7$ bar, $H_2/CO_2/Ar = 4/1/5$, 150 Nl h^{-1} g$^{-1}_{cat}$.

largest variance between experiment and prediction is discarded. The test is repeated with the retained models until no further model is rejected. The critical X_c^2-value is calculated according to ref. [41,42] and compared to the tabulated X_t^2-value with corresponding degrees of freedom and a probability level of 0.95.

3.2. Computational methods

The kinetics is integrated into an ideal plug flow reactor model. The ordinary differential equation is formulated as:

$$\frac{d\dot{n}_i}{dm} = v_i \cdot r$$

where $\dot{n}_i$ is the molar flow of component i, m the catalyst mass, v_i the stoichiometric coefficient of component i and r the reaction rate. By integration over the catalyst mass, directly the weighed catalyst sample is taken as integration limit and the exact bed volume is not needed. Athena Visual Studio® is employed for solving of the differential equations and parameter estimation. Its solver for ordinary differential equations is based on a Newton algorithm with a backward difference scheme for approximation of derivatives. Bayesian parameter estimation was chosen as provided by the built-in gregplus parameter estimation routine. For the parameter estimation the sum of squares of residuals of the integral methane production rate is minimized.

4. Results and discussion

4.1. Catalyst characterization

As shown by XRD analysis of the dried catalyst precursor samples, a Takovite structure is formed by coprecipitation, After calcination all reflections can be assigned to a NiO (Bunsenite) phase. Formation of $NiAl_2O_4$ spinel can only be observed after calcination, when the samples are exposed to temperatures >450 °C. The corresponding data and a more detailed XRD study are presented in the supporting part, as well as a TPR-TG analysis. The latter was used to identify the reductions parameters. It showed that a treatment at 500 °C for 8 h is sufficient to reduce completely to the active Ni.

Concerning the BET surface areas of the calcined samples (Table 4), NiAl11, NiAl13, NiAl15 show similar surface area compared to the pure alumina sample. Further increasing the nickel content, surface areas still remain rather large with values well above 100 m^2 g^{-1}, but are significantly lower in comparison to the alumina sample. The pure NiO sample with a surface area <30 m^2 g^{-1} emphasizes the importance of the precursor phase for the morphology after calcination.

The specific nickel surface area determined by H_2 chemisorption monotonically increases with the nickel content. A maximum value of 36.1 m^2 g^{-1} is obtained for sample NiAl51. Correlating the specific surface area with the Ni content, the Ni dispersion increases with the Ni content up to sample NiAl11 before reaching a plateau around 6% which corresponds to an average Ni crystallite size between 16 and 17 nm. Interestingly, a precursor structure of lower Ni content does not lead to a better dispersion of reduced Ni after calcination and reduction though one might expect a lower Ni fraction in the mixed oxide formed after calcination to result in smaller crystallites.

4.2. Kinetic measurements

4.2.1. Comparison of the catalysts

First, the weight time yield of methane production (WTY) is determined for the series of catalysts at a temperature of 260 °C at 7 bar total pressure and a 1/4/5 gas mixture of $CO_2/H_2/Ar$ with a total flow of 150 Nl h^{-1} g$^{-1}_{cat}$ immediately after reduction so that deactivation does not bias measurements and results can be correlated to H_2 chemisorption measurements of fresh catalysts. In these experiments as in all catalytic test runs, CO_2 was selectively reduced to methane. The CO content in the product gas is below 1000 ppm. Higher hydrocarbons, in particular ethane and propane, were detected by gas chromatography, however, in traces <50 ppm, close to the detection limit. For this reason, only the rate of methane formation is considered in the following and the reverse water-gas shift and chain-growth reactions are neglected.

Plotting the WTY measured immediately after reduction as a function of the specific nickel surface area determined by H_2 chemisorption (Fig. 1), a linear trend is found suggesting that the nickel surface acts as active site in the as-prepared catalysts. Furthermore, we do not observe any correlation between BET surface area and WTY. The linearity of specific Ni surface area and WTY also holds for samples of largely differing BET surface areas (128–235 m^2 g$^{-1}_{cat}$). This, however, does not necessarily mean the support does not influence the catalytic active phase, only the quantity of exposed surface area does not. Comparison of reaction rates
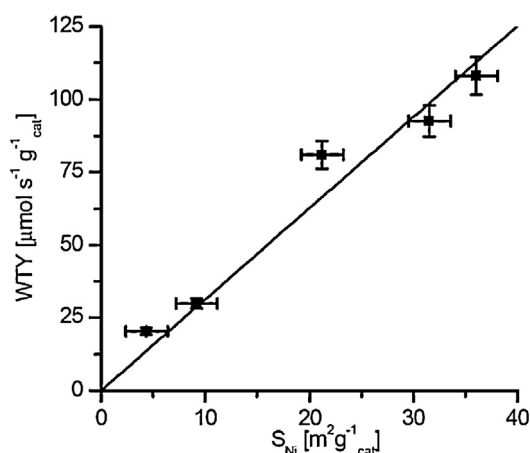
Fig. 1. Correlation between WTY ($p = 7$ bar, $T = 260\,°C$, $H_2/CO_2/Ar = 4/1/5$, 150 Nl h^{-1} g^{-1}$_{cat}$) and specific Ni surface area.

per Ni surface for different supports could clarify, if the nature of the support influences the specific activity or just the dispersion of Ni. In this regard, the degree of hydroxylation of the support is reported to affect the reactivity and selectivity in CO_2 hydrogenation [43]. Also adsorption of carbon dioxide on oxidic supports is in discussion in literature as possible role of the support in the methanation reaction. Aksoylu et al. [44], for instance, observed for a series of coprecipitated Ni/Al_2O_3 catalysts with a Ni content less than 25 wt.% that the methane production per Ni surface area rises with decreasing Ni content. This was attributed to carbon dioxide being also adsorbed on alumina, which via reverse spillover increases methane production per unit Ni surface especially for catalysts of low Ni loading. One might speculate if the high loadings of our samples prevents this effect to be observable throughout our series. The deviations to the linear trend as depicted in Fig. 1 do also not give rise to the conclusion that specific activity correlates with average crystallite size. Positive deviations are found both for the sample of largest crystallite size (NiAl15) and of NiAl11 with rather small Ni crystallites. The small number of samples and crystallite sizes above 15 nm, however, prohibit to draw any conclusions in regard of structure sensitivity and activity of flat surfaces versus steps and kinks. Concerning supported Ru catalysts it is reported that the turnover frequency of methane production increases by over an order of magnitude with increasing crystallite sizes from 2 to 4 nm, the effect, however, leveling off at higher sizes [45].

In the previous section, it has been shown that Ni dispersion of samples NiAl51, NiAl31 and NiAl11 is almost constant and higher than in samples of lower Ni content. If activity correlates linearly to Ni surface in the samples, highest yield per mass of Ni will be obtained for these samples. Since NiAl11 gives slightly higher WTY than predicted by the linear trend, this sample shows highest yield per mass of Ni concerning our samples (140 µmol s^{-1} g^{-1}$_{Ni}$). Hence we conclude, optimum Ni/Al ratio is above 1/1 under chosen preparation conditions to synthesize a catalysts with optimum performance in relation to Ni content. Lower Ni/Al ratios result in Ni particles of higher crystallite size (lower dispersion) so that activity related to Ni content is worse. Highest activity per catalyst mass is found for the sample with highest Ni content.

Correlation of the catalyst activity to specific surfaces is indispensable in our view, but has hardly be performed in literature for CO_2 methanation. To gain understanding on structure-activity relationships further catalysts will have to be prepared according to other techniques comprising also different oxidic carriers. Nevertheless, for the series of our coprecipitated catalysts the linearity between specific Ni surface area and WTY holds and hence encourages to develop a kinetic model for this kind of system. To set up a kinetic model, the catalyst NiAl11 was chosen.
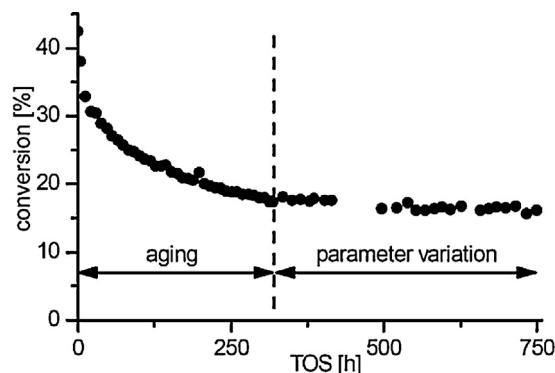

Fig. 2. Deactivation during aging and parameter variation.

4.2.2. Catalyst deactivation

For temperatures below 250 °C, the catalyst hardly showed any deactivation during parameter variation. However, in the measurements above 250 °C the catalyst activity rapidly dropped after the first data points with water already dosed in the feed. To decouple the kinetic measurements from deactivation phenomena, the catalyst was for this reason stressed before parameter variation: for a period of 320 h the reactor was fed with a mixture of $H_2/CO_2/H_2O/CH_4/Ar$ at 380 °C and 7 bar. It proved advantageous to feed product gases already in the feed during the formation period, since this way (i) a stable activity level could be reached faster than by feeding only carbon dioxide and hydrogen and (ii) kinetic measurements containing product gases in the feed did not cause further deactivation during parameter variation. During aging a reference point was measured periodically to track the decrease in activity since under aging conditions equilibrium was maintained and deactivation hence was not observable. After 320 h, parameter variation was started. The reference point was periodically measured between kinetic data points in order to ensure a stable activity level. As the reference measurements confirm (Fig. 2), the activity was stable after the aging period at around 40% of the initial activity during parameter variation so that measurements of kinetics used for parameter estimation are not biased by deactivation effects. It is a common feature of many published kinetics, that they do not relate to the initial activity, but to a stable level. Steam reforming kinetics by Xu and Froment [28], for instance, have to be multiplied by a factor of 2.2 to reflect initial activity. Concerning CO_2 methanation kinetics, most studies do not address deactivation, probably due to the fact that they were mostly measured under differential conditions and deactivation phenomena are less severe in this case according to our findings. Only Dew et al. [19] report on an extensive pretreatment (lasting over 2000 h) to maintain a stable activity in the following parameter variation. Abello et al. [29], who prepared a coprecipitated Ni/AlO_x with molar ratio of 5.4, report on a lifetime test at 400 °C. Conversion of carbon dioxide decreases from 92.4% to 83.5% during 490 h. Unfortunately, the initial conversion corresponds to equilibrium so that the decay does not reflect the decay in intrinsic activity. According to the kinetic model we present in Section 4.3.2 the decrease in conversion from 92.4% to 83.5% corresponds to a loss in intrinsic activity of more than 45%. This makes us conclude that the deactivation we observe is in the range of what has to be expected for the catalysts employed.

In order to check for reproducibility, the same aging procedure was performed on a second fresh catalyst fill. After 320 h the catalyst reached almost the same activity level according to measurements of the reference point. Subsequently a reduced data set was recorded on the deactivated catalyst. In Fig. 3 the two data sets are compared and a good agreement is observable. The overall deviation is calculated to 6.3%. As most data points are slightly above the angle bisector, the catalyst has obviously not been deac-
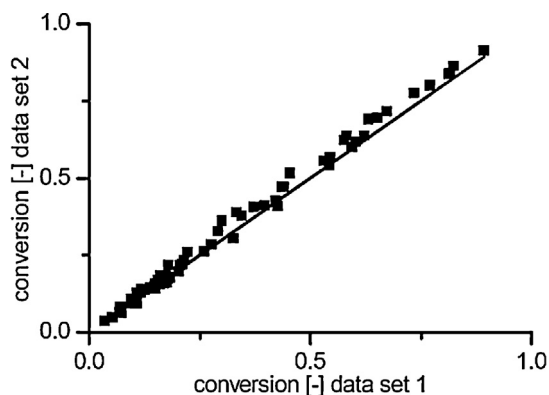
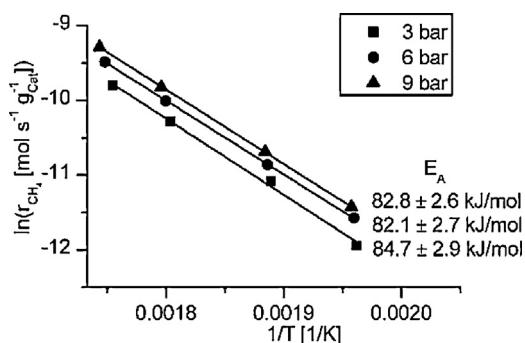**Fig. 3.** Comparison between first and second kinetic data set.

Fig. 4. Arrhenius plots at varying total pressures ($Q = 2400\,Nl\,h^{-1}\,g^{-1}_{cat}$, $H_2/CO_2/Ar = 1.6/0.4/8$, $m_{cat} = 25\,mg$).

tivated to exactly the same level. However, the experimental error within one data set might for this reason be even smaller than by comparing two data sets.

4.2.3. Apparent activation energy and reaction orders

The apparent activation energy for the CO_2 methanation reaction is within error tolerance independent of the total pressure and determined to $83\,kJ\,mol^{-1}$ (Fig. 4). This value is in line with literature where, for instance, values of 82 and $89\,kJ\,mol^{-1}$ are reported for Ni/SiO_2 [20,46], $80-106\,kJ\,mol^{-1}$ for Ni/Al_2O_3 [24,47] and $89\,kJ\,mol^{-1}$ for Ni(100) in a surface science approach [48].

According to Fig. 5, the apparent reaction orders of hydrogen and carbon dioxide are almost constant in the investigated temperature range and close to 0.3 and 0, respectively, for pure $H_2/CO_2/Ar$ feed streams (closed symbols). The reaction order of hydrogen seems to slightly rise at higher temperatures, which however might be caused by increased conversion and accordingly higher product gas contents at these temperatures. The comparison to measurements with product gases already dosed in the feed stream reveals
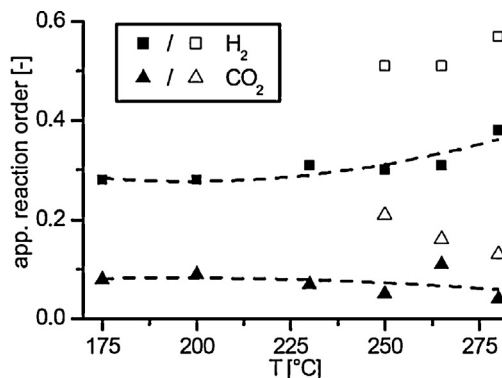

Fig. 5. Apparent reaction orders of H_2 and CO_2 closed symbols: $H_2/CO_2/Ar$ feed, open symbols: $H_2/CO_2/H_2O/CH_4/Ar$ feed.

a marked increase in apparent reaction orders of both hydrogen and carbon dioxide (open symbols). Apparently, the presence of product gases will slow down the reaction rates more severely at depleting hydrogen and carbon dioxide contents. The trends of reaction orders for pure feed gas in absence of product gases are in accordance with the study of Weatherbee and Bartholomew: they report increasing (decreasing) reaction orders of hydrogen (carbon dioxide) with temperature in the range of 0.35–0.55 (0.24–0.07) at low partial pressures while both hydrogen and carbon dioxide dependence approach zero-order at higher partial pressures [20]. Similarly, van Herwijnen et al. report zero-order dependence of carbon dioxide at partial pressures above 0.015 atm [24].

4.3. Kinetic rate equations

4.3.1. Power law rate equations

Based on the extensive dataset as described in the experimental section and recorded at TOS > 320 h (cf. Fig. 2), parameters of the different rate equations were estimated. Fig. 6 compares the parity plots of the integral methane production rate for PL, PL–H2O and PL–HI. PL–WI gives results similar to PL–HI with slightly higher residual so that it is not further considered. The parity plot of PL shows a wide spread compared to the experimental values and a mean absolute residual of over 20%. Consequently, it is inadequate to reflect the kinetics over the whole range of conditions employed. Nevertheless, this model allows an excellent description of data points with differential conversion in absence of product gases over the whole temperature and pressure range. However, as soon as product gases are present in larger amounts, it systematically overestimates reaction rates and fails in describing the slow approach to equilibrium experimentally observed. On the one hand this emphasizes the need for more complex models that should be suitable for reactor modeling in technical scale, where the description of the approach to equilibrium is crucial for reactor design [49], and on the other hand the demand of kinetic measurements that
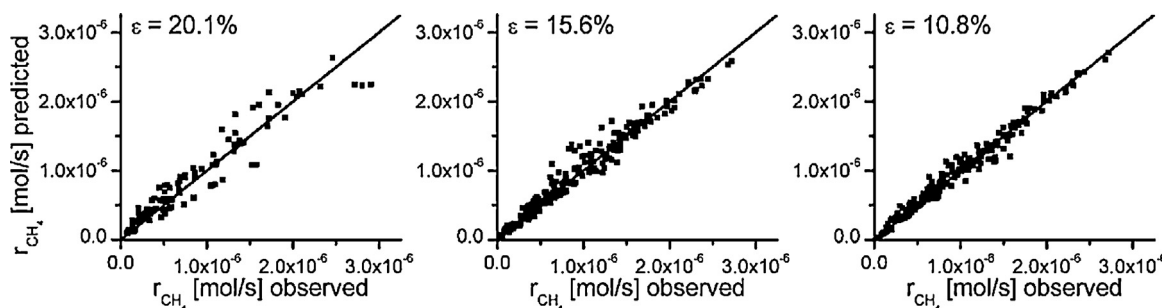

Fig. 6. Parity plots for PL, PL-H2O and PL-HI (from left to right).
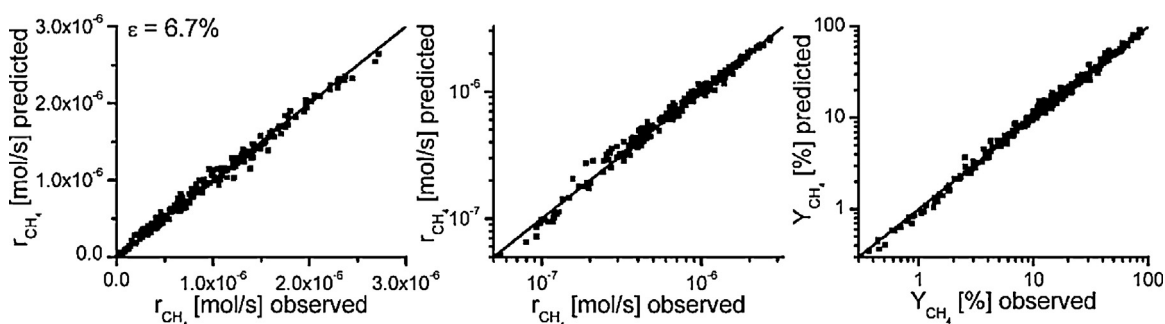
Fig. 7. Parity plots for LHHW rate equation. Left: integral methane production rate, center: logarithmic methane production rate, right: yield of methane.

Table 5
Parameter estimation for PL-HI (T_{ref} = 555 K).

$k_{0,555K}$	$6.41e{-}05 \pm 3.0e{-}6$	mol bar$^{-0.54}$ s^{-1} g$_{cat}$$^{-1}$
E_A	93.6 ± 2.5	kJ mol^{-1}
n_{H2}	0.31 ± 0.02	–
n_{CO2}	0.16 ± 0.02	–
$A_{OH,555K}$	0.62 ± 0.09	bar$^{-0.5}$
ΔH_{OH}	64.3 ± 6.3	kJ mol^{-1}

have to cover conditions closer to equilibrium. For this reason, the dataset contains measurements where water and methane have been fed already in the gas supply and the reactor is operated in an integral mode. An inhibiting influence of product gases has been observed before by Kai et al. [20] by comparing methanation rates in a differential and integral reactor. Concerning Ru systems it has also been reported that addition of water shifts conversion temperature curves to higher temperatures, which means reaction rates are decreased in presence of water [45].

To the best of our knowledge, empirical power law equations for the methanation of carbon dioxide, which consider a retarding influence of water, have not been described in literature, probably because most studies address differential conversion with very low product gas contents. Similar empirical power law models as adopted here have, however, been successfully employed for methanol synthesis, for instance [50]. Parameter estimation for PL–H2O yields a negative reaction order, which reflects the inhibiting influence mentioned above. The residual is consequently considerably decreased. Nevertheless, the comparison to PL–WI emphasizes that the assumption of a constant reaction order of water over the whole temperature and pressure range proves restrictive. In contrast, PL–WI and in particular PL–HI are found superior since the reaction rate is even more drastically slowed down near equilibrium. The low mean absolute residual suggests PL–HI to be an adequate and meanwhile very simple model for reflection of kinetics from differential conversion to almost complete conversion in thermodynamic equilibrium. The parameters for PL-HI are summarized in Table 5. The confidence intervals are rather small and show all parameters to be estimated significantly different from 0.

4.3.2. LHHW rate equations

The following rate equation, which has been derived by assuming formyl formation as rate determining step in mechanism b, proved best in a statistically significant way according to Bartlett's test. All other models (including all power law rate equations) could be rejected on basis of the dataset comprising 258 experiments.
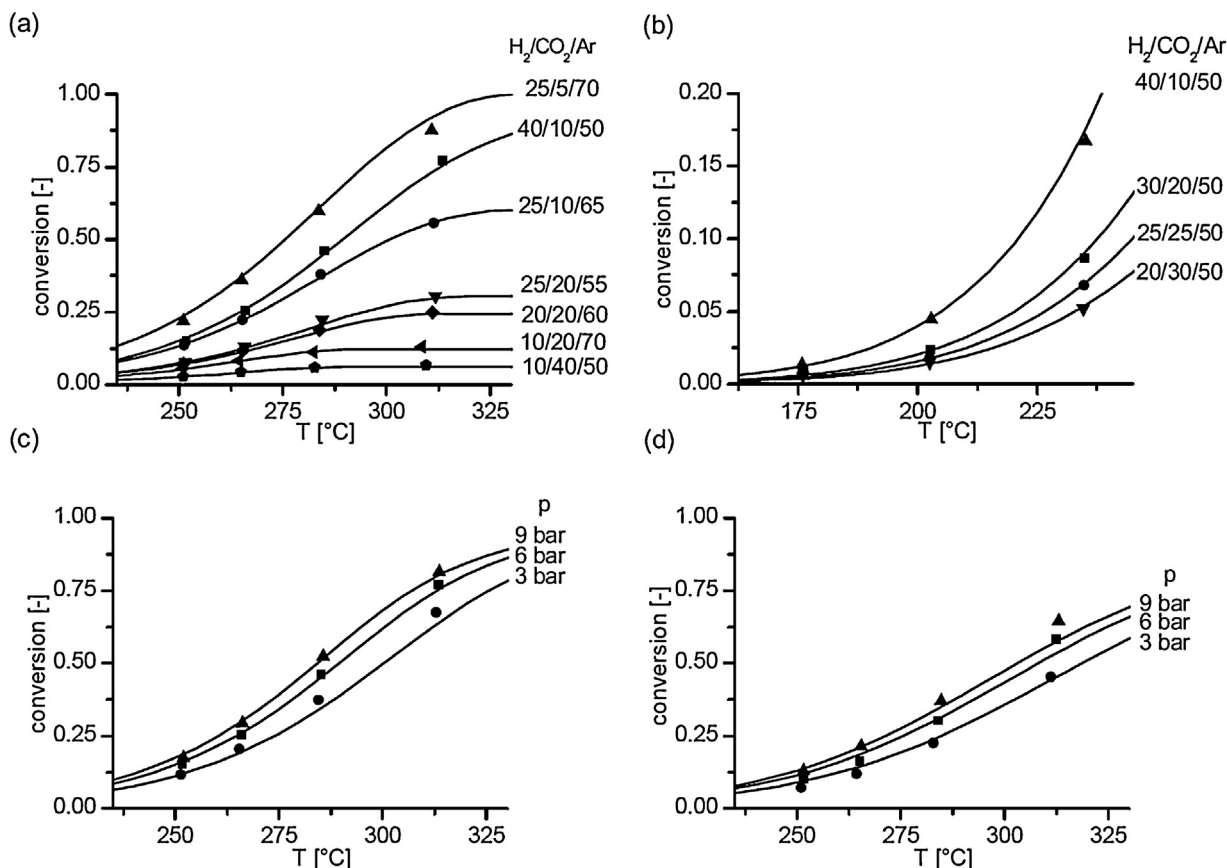
$$r = \frac{k \cdot p_{H_2}^{0.5} p_{CO_2}^{0.5} \left(1 - \frac{p_{CH_4} p_{H_2O}^2}{p_{CO_2} p_{H_2}^4 K_{eq}} \right)}{\left(1 + K_{OH} \frac{p_{H_2O}}{p_{H_2}^{0.5}} + K_{H_2} p_{H_2}^{0.5} + K_{mix} p_{CO_2}^{0.5} \right)^2}$$

Nevertheless, based on stationary measurements in a lab scale fixed-bed reactor, any inference to the mechanism prevalent seems very doubtful without identification of surface species, a comparison to specific rate constants measured under UHV conditions or quantum mechanical calculations etc. Apart from that, several identical rate equations could be derived for mechanisms a and b. This emphasizes the ambiguity about inferring the mechanism with the strict assumptions required for derivation of simple LHHW-type rate equations. Furthermore, the rate equation derived from mechanism b with formyl HCO formation as rate determining step is identically derived by assuming the formation of carbon–hydroxyl COH as rate determining and subsequent cleavage to adsorbed carbon and OH in analogy to the mechanism of CO cleavage according to ref. [35]. Those types of simple LHHW rate equations, however, have been adopted for describing and also extrapolating the kinetics of various reactions though the exact mechanism is not known except for few examples.

Fig. 7 shows the parity plot for the selected LHHW rate equation. The data are predicted very well by the model with a mean absolute residual of 6.7%. As illustrated in the log-scale plot, the smallest methane formation rates are slightly systematically underestimated, which, however, is hardly accounted for in the parameter estimation because of the small absolute values. The mole fractions of methane of those values are below 1%. Apart from that, no systematic deviations are observable in the parity plots. For comparison, also the parity plots of yield related to carbon dioxide are given in order to show that the experiments cover the whole range from differential to almost complete conversion. Fig. 8(a) and (b) report conversion in dependence of feed temperature and highlight the model's capability of reflecting H_2/CO_2 ratios over more than one order of magnitude very accurately. In agreement to determined reaction orders in Section 4.2.3, the dependence of total pressure on reaction rates is rather low as depicted in Fig. 8(c). Maintaining the same partial pressures of both reactants and experimental conditions, but feeding water and methane in addition slows down reaction rates considerably (Fig. 8(c) and (d)). For instance, at a total pressure of 9 bar and temperature of 285 °C, conversion of carbon dioxide is reduced from 53% to 37%, which is also captured by the model. If a model is adopted to technical SNG production, where water contents towards the reactor end will range in excess of 50 mol%, it will be crucial that the inhibiting effect of products is adequately represented by the model. Hence, all models parameterized on basis of initial reaction rates in absence of product gases will fail in this respect.

The estimated parameters for the selected LHHW rate equations are given in Table 6. The 95% confidence intervals are rather large, in general. In particular, the adsorption enthalpy of H_2, ΔH_{H2}, is not significantly different from 0. Hence, one might argue that the model contains an excessive number of parameters to describe the experiments in the data set. However, in contrast to the power law rate equations, the model predictions are significantly better. Using
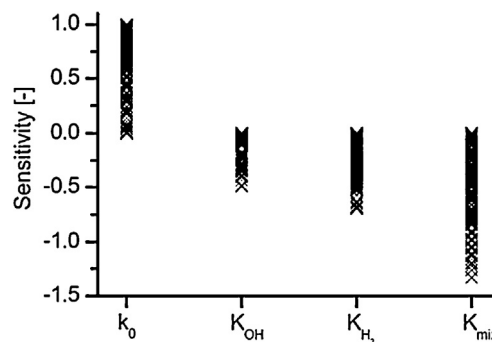
Fig. 8. Comparison of experimental results (points) and model predictions (lines).
(a) H_2/CO_2 ratio ($Q = 120$ Nl h^{-1} g^{-1}$_{cat}$, $m_{cat} = 25$ mg, $p = 6$ bar),
(b) H_2/CO_2 ratio ($Q = 48$ Nl h^{-1} g^{-1}$_{cat}$, $m_{cat} = 75$ mg, $p = 4$ bar),
(c) Total pressure ($Q = 120$ Nl h^{-1} g^{-1}$_{cat}$, $m_{cat} = 25$ mg, $H_2/CO_2/Ar = 40/10/50$),
(d) Total pressure ($Q = 120$ Nl h^{-1}g^{-1}$_{cat}$, $m_{cat} = 25$ mg, $H_2/CO_2/CH_4/H_2O/Ar = 40/10/12.5/25/12.5$).

Table 6
Parameter estimation for LHHW rate equation ($T_{ref} = 555$ K).

$k_{0,555K}$	3.46e-4 ± 4.1e-5	mol bar^{-1} s^{-1} g$_{cat}$$^{-1}$
E_A	77.5 ± 6.9	kJ mol^{-1}
$A_{OH,555K}$	0.50 ± 0.05	bar$^{-0.5}$
ΔH_{OH}	22.4 ± 6.4	kJ mol^{-1}
$A_{H2,555K}$	0.44 ± 0.08	bar$^{-0.5}$
ΔH_{H2}	−6.2 ± 10.0	kJ mol^{-1}
$A_{mix,555K}$	0.88 ± 0.10	bar$^{-0.5}$
ΔH_{mix}	−10.0 ± 5.7	kJ mol^{-1}

Fig. 9. Local sensitivity analysis for LHHW rate equation for all measurements of the data set.

Bartlett's test, all power law equations are rejected in comparison to the selected LHHW models despite the smaller number of parameters. The local sensitivities of the parameters calculated for all data points (Fig. 9) emphasize all parameters affect the reaction rates (see Appendix for calculation of sensitivities). Descriptively, a sensitivity of 1 for a parameter means that an increase of this parameter by 1% increases the overall reaction rate by 1%. Correspondingly, parameters with local sensitivity 0 do not affect the reaction rate under chosen reaction conditions, while negative sensitivities correspond to parameters which, if increased, slow down reaction rates. That the rate constant k_0 shows a sensitivity close to zero for few data points is due to the approach to equilibrium. K_{OH} affects the reaction rates at high water contents whereas it has hardly any influence at differential conversions. As discussed above, the apparent reaction order of carbon dioxide can be approximated close to zero increasing with approach to equilibrium. In the LHHW rate equation this is reflected by K_{mix}. With decreasing partial pressure of carbon dioxide the apparent reaction order in the

model approaches 0.5 according to the exponent of carbon dioxide in the numerator.

For validation, the model predictions are compared to conversion temperature plots for the feed gas composition $H_2/CO_2/Ar = 4/1/5$ for pressures of 8 bar in the temperature range from 180 °C to 450 °C (Fig. 10). The conversion is reflected adequately over the whole temperature range. In particular, the model captures the slowed approach to thermodynamic equilibrium in contrast to simple power law model comprising only exponents for hydrogen and carbon dioxide (PL).

Fig. 11 compares our kinetic model to predictions by several models from literature. The most obvious feature is that kinetics measured on our coprecipitated system are considerable faster
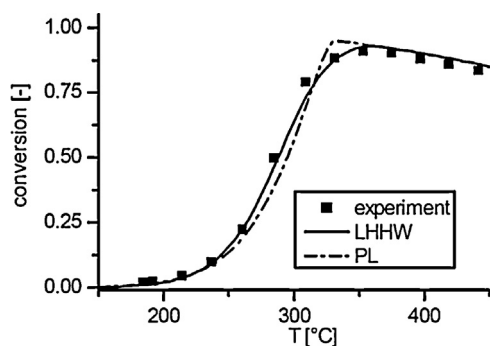
Fig. 10. Conversion-temperature plot for $H_2/CO_2/Ar = 4/1/5$, $p = 8$ bar, $Q = 150$ Nl h^{-1} g^{-1}$_{cat}$, $m_{cat} = 25$ mg.
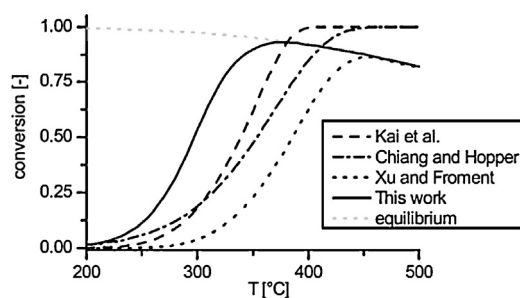

Fig. 11. Comparison to predictions by kinetics from literature.

than predicted by literature models. Consequently, we can confirm the conclusion by Abello et al. [29], who proposed coprecipitated high-loaded Ni/Al$_2$O$_3$ for CO$_2$ methanation. They also found their catalyst (molar ratio Ni/Al = 5.4) superior to literature systems. In relation to the model by Kai et al. [27], the high activity, however, seems plausible: with a 17 wt.% Ni/La$_2$O$_3$/Al$_2$O$_3$ they employed a considerably less loaded system than the coprecipitated 58 wt.% NiAl(O)$_x$ of this work. Also slopes of the conversion temperature plots are alike, which indicates that apparent activation energies are similar. The power law kinetics by Chiang and Hopper [25] deviate in this respect. The 15 wt.% Ni steam reforming catalyst adopted by Xu and Froment [28] for methanation experiments is considerably less active. Conversion temperature plots are shifted by about 50 °C to higher temperatures. We showed in a previous study that predictions by Xu and Froment's model are close to experimental results for an impregnated 5 wt.% Ni/ZrO$_2$ catalyst [49]. Fig. 11 also emphasizes that it is indispensable to consider the thermodynamic equilibrium if the models are to be adopted for simulation of reactors intended for production of pure SNG. Not only is our model capable of capturing the equilibrium, but the approach to equilibrium is also described adequately due to the extensive dataset for parameter estimation. In comparison to previous kinetic models from literature as listed in Table 1 our model for the first time combines the reflection of intrinsic (i) kinetics on a state-of-the-art catalyst system (ii) under industrially relevant conditions (iii) in terms of pressure, temperature and feed composition.

5. Conclusion

A series of catalysts with varying Ni/Al ratio has been prepared by coprecipitation. After calcination of the hydrotalcite-like precursors, a mixed oxide phase ('disordered oxide-spinel intermediate') was formed during calcination at 450 °C. After reduction, specific nickel surface areas were measured by H$_2$ chemisorption. Nickel surface areas increased with Ni content, while average Ni particle sizes according to chemisorption and elementary analy-

sis decreased with higher Ni content up to about 50 wt.% Ni before reaching a constant value around 17 nm.

The main conclusions of the kinetic characterization and modeling are:

(3) A simple power law allows for an excellent description at differential conversions and pure H$_2$/CO$_2$ feed streams. Reaction orders of 1/3 and close to zero are found for hydrogen and carbon dioxide, respectively, for a wide range of conditions. However, the power law systematically overestimates reaction rates while approaching the thermodynamic equilibrium.

(4) By Introducing an empirical inhibition term concerning adsorbed water or preferable hydroxyl – both are similarly derived in the LHHW approaches – the kinetics can be reflected from differential to almost complete conversion for all reaction conditions applied in this study.

(5) LHHW-type rate equations are best suited to describe the kinetics. Compared to the power law approaches comprising inhibition, the residuum is significantly lowered, however at the expense of a larger number and wider confidence intervals of the parameters. Though best results were obtained for rate equations derived on the assumption of a hydrogen assisted carbon oxygen bond cleavage, conclusions on the mechanism are not drawn solely based on our dataset comprising stationary experiments.

In view that coprecipitated NiAl(O)$_x$ is regarded as promising catalyst system for the methanation of carbon dioxide, our work encourages also to further investigate aspects that aroused during our kinetic study, that is i.a. the influence of the calcination temperature and spinel formation on structure, reducibility and stability during reaction, deactivation phenomena like sintering, coking or structural changes and in particular the influence of water thereon. Finally, further mechanistic insight needs to be gained to support the development of a comprehensive elementary step kinetic model. This relates in particular to the open question of a direct CO$_2$ methanation route or a consecutive pathway with CO intermediate and to the influence of hydrogen on C—O bond cleavage. Since proposed elementary reactions in literature are very similar to the ones of methane reforming reactions, it might be a promising approach to adopt these elementary step kinetic models derived and parameterized for reforming [51,52] to the methanation reaction for mechanistic insights.

Appendix A.

A.1. Assessment of transport limitations

For all criteria, gas phase properties were calculated on basis of the feed gas composition. The thermal conductivity of the gas phase was approximated by the rule of Wassiljeva based on data provided in VDI-Wärmeatlas [53]. As diffusion coefficient, the binary diffusion coefficient of carbon dioxide in hydrogen was assumed. Concerning the effective diffusion coefficient for the Weisz-Prater criterion also Knudsen diffusion of CO$_2$ was considered next to molecular diffusion according to the Bosanquet formula. The cata-

lyst density and effective thermal conductivity were approximated with 2300 kg m^{-3} and 0.15 W m^{-1} K^{-1}, respectively. Heat and mass transfer coefficients were estimated by correlation equations [54]. Measured integral methane formation rates are inserted as effective reaction rates r^{eff}. Following criteria have been checked for all data points in the parameter variation:

Intraparticle mass transport — Weisz-Prater criterion [55]

$$\frac{r^{eff}\rho_{cat}d_{cat}^2}{4c_{CO_2}D_{CO_2}^{eff}} < 1$$

Intraparticle heat transport — Anderson criterion [56]

$$\frac{r^{eff}|\Delta H|\rho_{cat}d_{cat}^2}{4\lambda^{eff}T} < \frac{0.75RT}{E_A}$$

External mass transport — Mears criterion [57]

$$\frac{r^{eff}\rho_{cat}d_{cat}}{h_m c_{CO_2}} < 0.3$$

External heat transport — Mears criterion [57]

$$\frac{r^{eff}|\Delta H|\rho_{cat}d_{cat}}{h_t T} < \frac{0.3RT}{E_A}$$

A.2. Derivation of LHHW kinetic rate equations

The kinetic rate equations are derived analogously to the methodology of reference [20] which has also been adopted by Kopyscinsky et al. [31,32] for the case of CO methanation. Exemplarily, the derivation will be presented for mechanism b assuming step 3 as rate determining and treating step 8 as irreversible.

The overall reaction rate is equal to the rate of elementary step 3, the formation of the formyl species, which is considered as rate determining step:

$$r = k_3 \Theta_{CO}\Theta_H$$

θ_H and θ_{CO} are the coverages of hydrogen and carbon monoxide, respectively, k_3 is the forward rate constant of elementary step 3. The coverage of hydrogen is easily accessible by assuming dissociative Langmuir adsorption that is in quasi-equilibrium:

$$k_2 p_{H_2}\Theta_*^2 = k_{-2}\Theta_H^2$$

$$\Theta_H = \sqrt{K_{H_2}p_{H_2}}\,\Theta_*$$

K_{H2} represents the equilibrium constant of reaction 2 and θ_* the fraction of free surface sites. Adsorbed carbon monoxide stems from dissociative adsorption of carbon dioxide which is also assumed as Langmuir adsorption in quasi-equilibrium:

$$k_1 p_{CO_2}\Theta_*^2 = k_{-1}\Theta_{CO}\Theta_O$$

$$\Theta_{CO} = K_{CO_2}p_{CO_2}\frac{\Theta_*^2}{\Theta_O}$$

At steady state, the rate of oxygen hydrogenation must be twice the rate of the rate determining step. Furthermore, it is assumed that the equilibrium of reaction 7 is shifted far to the right, so this reaction can also be treated as irreversible.

$$\frac{d\Theta_O}{dt} = 0 \Rightarrow r_7 = 2r_3$$

$$r_7 \approx k_7\Theta_O\Theta_H$$

$$k_7\Theta_O\Theta_H = 2k_3\Theta_{CO}\Theta_H$$

$$\Theta_O = \frac{2k_3}{k_7}\Theta_{CO}$$

Inserting in the equation above finally results in the coverage of CO:

$$\Theta_{CO} = \sqrt{\frac{k_7}{2k_3}K_{CO_2}p_{CO_2}}\,\Theta_*$$

The reaction rate can now be expressed as:

$$r = k_3\sqrt{\frac{k_7}{2k_3}K_{CO_2}p_{CO_2}K_{H_2}p_{H_2}}\,\Theta_*^2$$

Assuming hydrogen, carbon monoxide and hydroxyl as most abundant surface intermediates (MASI) the balance over the adsorption sites can be formulated as follows:

$$1 = \Theta_H + \Theta_{CO} + \Theta_{OH} + \Theta_*$$

Assuming steps 8 and 9 in equilibrium the coverage of hydroxyl can be expressed as

$$\frac{K_8}{K_{H_2O}} = \frac{p_{H_2O}\Theta_*^2}{\Theta_H\Theta_{OH}}$$

$$\Theta_{OH} = \frac{K_{H_2O}p_{H_2O}}{K_8\sqrt{K_{H_2}p_{H_2}}}\Theta_*$$

Finally, the fraction of free surface sites can be formulated as function of known variables:

$$\Theta_* = \frac{1}{1 + \sqrt{K_{H_2}p_{H_2}} + \sqrt{\frac{k_7}{2k_3}K_{CO_2}p_{CO_2}} + \frac{K_{H_2O}p_{H_2O}}{K_8\sqrt{K_{H_2}p_{H_2}}}}$$

Considering the thermodynamic equilibrium, the reaction rate results in

$$r = \frac{k_3\sqrt{\frac{k_7}{2k_3}K_{CO_2}p_{CO_2}K_{H_2}p_{H_2}}\left(1 - \frac{p_{CH_4}p_{H_2O}^2}{K_{eq}p_{CO_2}p_{H_2}^4}\right)}{\left(1 + \sqrt{K_{H_2}p_{H_2}} + \sqrt{\frac{k_7}{2k_3}K_{CO_2}p_{CO_2}} + \frac{K_{H_2O}p_{H_2O}}{K_8\sqrt{K_{H_2}p_{H_2}}}\right)^2}$$

Grouping the constants for convenience, the reaction rate is written as:

$$r = \frac{kp_{CO_2}^{0.5}p_{H_2}^{0.5}\left(1 - \frac{p_{CH_4}p_{H_2O}^2}{K_{eq}p_{CO_2}p_{H_2}^4}\right)}{\left(1 + \sqrt{K_{H_2}p_{H_2}} + K_{mix}p_{CO_2}^{0.5} + K_{OH}\frac{p_{H_2O}}{p_{H_2}^{0.5}}\right)^2}$$

If instead of hydroxyl water is assumed as MASI, the last term in the denominator is replaced accordingly:

$$r = \frac{kp_{CO_2}^{0.5}p_{H_2}^{0.5}\left(1 - \frac{p_{CH_4}p_{H_2O}^2}{K_{eq}p_{CO_2}p_{H_2}^4}\right)}{\left(1 + \sqrt{K_{H_2}p_{H_2}} + K_{mix}p_{CO_2}^{0.5} + K_{H_2O}p_{H_2O}\right)^2}$$

Table S.1 in the supporting information pools all rate equations that have been derived assuming water as MASI. Where appropriate, also OH has been accounted for as MASI (not listed). Concerning mechanism a, steps 1, 3, 4, 5 and 7 have been set as RDS, respectively. All other steps have been assumed as equilibrated (Case 1), or step 7, the hydrogenation of oxygen (Case 2), or step 8, the hydrogenation of OH (Case 3), have been assumed as irreversible. Concerning mechanism b, steps 4 and 5 have been assumed as RDS.
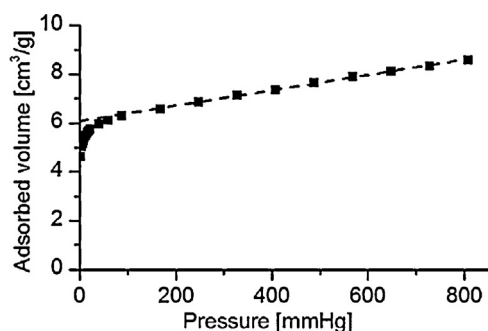
Fig. A1. Chemisorption measurement for NiAl11.

A.3. Calculation of specific surface area, dispersion and average crystallite size following the extrapolation theory

During chemisorption measurements the adsorbed gas volume depending on the pressure is determined. Molecules are not only adsorbed by chemisorption, but also by physisorption, which linearly depends on pressure. In the experiment, as shown exemplarily in Fig. A1 for the NiAl11, the combination of chemisorption and physisorption is measured. To extract the chemisorbed gas volume, the linear part of the combined curve above pressures of 200 mmHg is extrapolated to zero pressure and the y-axis intercept is determined.

The specific surface area A_{sp} is calculated following the equation:

$$A_{sp} = n_{ads} \cdot \nu \cdot A_m$$

Wherein n_{ads} is the amount of adsorbed molecules, ν the stoichiometry factor (2 for H_2-chemisorption), and A_m the cross section of the active species ($A_{Ni} = 6.49\,Å^2$). To determine the dispersion D of the active species, the equation

$$D = \frac{n_{ads} \cdot \nu M}{w}$$

is applied. M represents the molecular weight of Ni and w its weight fraction. The average crystallite size d is calculated according to

$$d = \frac{w \cdot f}{A_{sp} \cdot \rho}$$

with f as the shape correction factor (here 6 for spherical particles), ρ as density of Ni ($8.9\,g\,cm^{-3}$) (DIN 66,136–1).

A.4. Calculation of local sensitivities

Local sensitivities are approximated by finite differences in form of a relative sensitivity coefficient:

$$S_i = \frac{par_i}{r_{CH_4}} \frac{\partial r_{CH_4}}{\partial par_i} = \lim_{\Delta par_i \to 0} \frac{r_{CH_4,var} - r_{CH_4,ref}}{r_{CH_4,ref} \cdot var}$$

par_i corresponds to the parameter of interest and var to the respective variation, which was chosen as 1%.

A.5. Further characterization by a detailed XRD Study of the NiAl(O)$_x$ Catalysts

Fig. A2 (left) shows the XRD patterns for the dried precursors with varying Ni/Al ratio. Concerning samples NiAl51 and NiAl31 all reflections can be assigned to Takovite (JCPDS 15-0087), a member of the hydrotalcite structure. Decreasing the Ni/Al ratio to 1, the main reflection at $2\theta = 11.7°$ representing the (0 0 3) plane disappears completely while the reflection assigned to (0 0 6) plane at 23.5° is still present, however in very low intensity. The reflections at 37.4° and 61.1° in NiAl51 are gradually shifted to lower plane distances with increasing Al^{3+} content. Samples NiAl13 and NiAl15 show a new reflection at 20.4°. The comparison to Al^{3+} precipitated under the same conditions in absence of Ni^{2+} (not shown) reveals that the crystalline phase present in NiAl13 and NiAl15 requires Ni^{2+} since the reflections in the reference diffractogram can all be assigned to Boehmite (γ-AlO(OH)) (JCPDS 21-1307) which is not detected in the binary NiAl samples. Generally, if precipitated fast in alkaline solutions Al^{3+} is expected to crystallize as metastable hexagonal α-aluminum hydroxide (Bayerite) which transforms to more stable γ-aluminum hydroxide (Gibbsite) [58]. Both phases are not detected in the precursor samples, either.

After calcination (Fig. A2 center), all reflections in sample NiAl51 can be assigned to a NiO (Bunsenite) phase (JCPDS 78-0429). No separate crystalline alumina phases are detected. With increasing Al content, the intensity decreases and the reflections at 43.6° and 63.3° in NiAl51 are gradually shifted to lower plane distances. Interestingly, already the reflections in NiAl51 are slightly shifted compared to the expected values of pure NiO. The results for variation of the calcination temperature for NiAl11 in Fig. A2 (right) shed light on this effect: with increasing calcination temperature a NiAl$_2$O$_4$ spinel phase (JCPDS 10-0339) is identified next to Bunsenite. Bunsenite crystallizes in NaCl structure, accordingly O^{2-} is located in fcc positions while Ni^{2+} occupies the octahedral vacancies. NiAl$_2$O$_4$ is reported as a (disordered) spinel structure with preference to the inversed configuration [59]. Hence, O^{2-} is also positioned in fcc where 1/8 of tetrahedral vacancies is preferably occupied by Al^{3+} while Ni^{2+} and the remaining Al^{3+} are located in 1/2 of octahedral vacancies. The cubic lattice parameter of Bunsenite and NiAl$_2$O$_4$ are 4.2 and 8.0 Å where in the latter one elementary
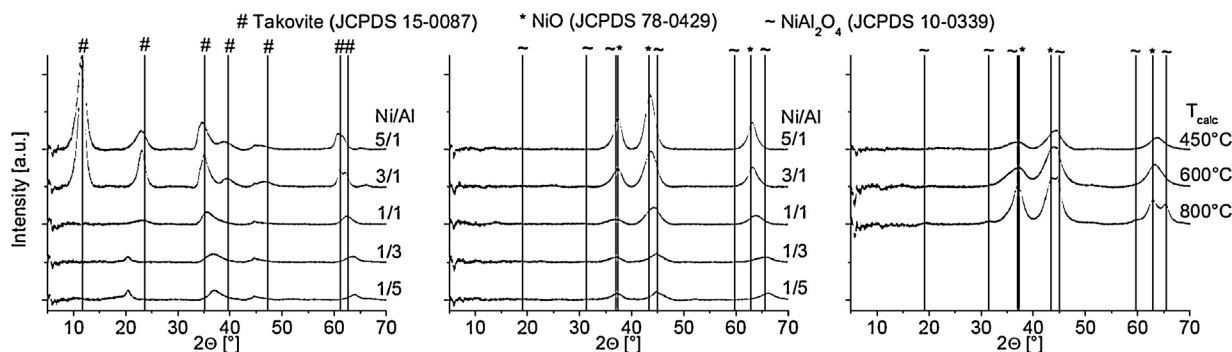

Fig. A2. XRD patterns: precursors after drying at 80 °C overnight (left), after calcination at 450 °C (center), variation of calcination temperature for sample NiAl11 (right).
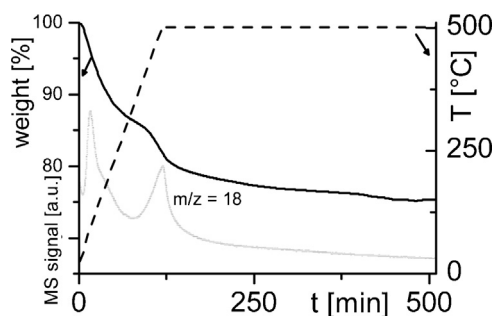
Fig. A3. Temperature programmed reduction of NiAl11.

cell, however, comprises eight times the number of O^{2-}. Hence, the proximity of the main reflection positions of both phases results directly from the similarity of the structures and the little smaller lattice parameters in case of the spinel. One might speculate whether already after calcination at $450\,^\circ$C a spinel phase of low crystallinity and grain size is present besides other oxidic Al_2O_3 and NiO phases or a mixed oxide is formed which shifts the reflections with increasing Al content. For instance, de Korte et al. also studied the calcination of similarly prepared precursors and named the mixed oxide phases with plane distances between NiO and $NiAl_2O_4$ as DOSI ('disordered oxide-spinel intermediate') and those with plane distances between $NiAl_2O_4$ and Al_2O_3 as NCA ('nickel oxide containing alumina') [60]. Noteworthy, γ-Al_2O_3 (formed after calcination of the pure Al sample (not shown)) crystallizes in a defect spinel structure with a lattice parameter of 7.9 Å. This might be the reason why the reflection at 66.2° in NiAl15 is slightly shifted to higher angles compared to the (440) reflection of $NiAl_2O_4$, e.g., measured on the sample calcined at $800\,^\circ$C at 65.5° and expected at 65.5°.

The reduction of the calcined samples has also been studied by TPR (Fig. A3). While heating in a hydrogen argon flow, first carbon dioxide and water are desorbed at temperatures $<350\,^\circ$C. In view of the calcination at $450\,^\circ$C before reduction, this suggests that carbon dioxide might have been adsorbed on basic oxides or hydroxides during exposure of the calcined catalyst in air. The water formation above $350\,^\circ$C follows from reduction to metallic Ni. To test for complete reduction, a TG–MS was measured with the catalyst overflowed by pure argon instead of hydrogen in argon. The first stage of decomposition accompanied by the release of carbon dioxide and water is identical. However, no further water is released above $350\,^\circ$C. The difference of the samples' masses after treatment at $500\,^\circ$C amounts to 9.1%. Based on the Ni/Al ratio determined in elementary analysis of the corresponding precursor, a mass loss of 8.8% is expected, assuming the calcined sample as pure NiO/Al_2O_3. We conclude that NiO is completely reduced within the error tolerance of the TG–MS measurements. Noteworthy this is not the case if the catalyst is calcined at higher temperatures and a spinel phase is formed. Before kinetic measurements, it is also checked that reduction is complete by monitoring that no more water is released.

Appendix A. Supplementary data

Supplementary data associated with this article can be found, in the online version, at http://dx.doi.org/10.1016/j.apcatb.2015.07.026.

References

[1] A Roadmap for moving to a competitive low carbon economy in 2050, European Commision, 2011.
[2] M. Sterner, Bioenergy and Renewable Power Methane in Integrated 100% Renewable Energy Systems, PhD Thesis Kassel University, 2009.
[3] M. Specht, J. Brellochs, V. Frick, B. Stürmer, U. Zuberbühler, M. Sterner, G. Waldstein, Erdöl Erdgas Kohle 126 (2010) 342–346.
[4] S. Schiebahn, T. Grube, M. Robinius, L. Zhao, A. Otto, B. Kumar, M. Weber, D. Stolten, Transition to Renewable Energy Systems, Wiley-VCH, 2013, pp. 813–848.
[5] M. Streibel, N. Nakaten, T. Kempka, M. Kühn, Energy Procedia 40 (2013) 202–211.
[6] Audi Press Release. World premiere: Audi opens power-to-gas facility, 2013.
[7] J. Gao, Y. Wang, Y. Ping, D. Hu, G. Xu, F. Gu, F. Su, RSC Adv. 2 (2012) 2358–2368.
[8] P. Sabatier, J. Senderens, Compt. Rend. 134 (1902) 689–691.
[9] H. Kusama, K.K. Bando, K. Okabe, H. Arakawa, Appl. Cat. A 197 (2000) 255–268.
[10] E. Novak, K. Fodor, T. Szailer, A. Oszkó, A. Erdöhelyi, Top. Catal. 20 (2002) 107–117.
[11] A. Beuls, C. Swalus, M. Jacquemin, G. Heyen, A. Karelovic, P. Ruiz, Appl. Cat. B 113 (2012) 2–10.
[12] E. Zağli, J.L. Falconer, J. Catal. 69 (1981) 1–8.
[13] K.P. Brooks, J. Hu, H. Zhu, R.J. Kee, Chem. Eng. Sci. 62 (2007) 1161–1170.
[14] T. Abe, M. Tanizawa, K. Watanabe, A. Taguchi, Energ. Environ. Sci. 2 (2009) 315–321.
[15] D. Li, N. Ichikuni, S. Shimazu, T. Uematsu, Appl. Cat. A 180 (1999) 227–235.
[16] M. Schoder, U. Armbruster, A. Martin, Chem. Ing. Tech. 85 (2013) 344–352.
[17] J.-N. Park, E.W. McFarland, J. Catal. 266 (2009) 92–97.
[18] H.Y. Kim, H.M. Lee, J.-N. Park, J. Phys. Chem. C 114 (2010) 7128–7131.
[19] J. Dew, R. White, C. Sliepcevich, Ind. Eng. Chem. 47 (1955) 140–146.
[20] G.D. Weatherbee, C.H. Bartholomew, J. Catal. 77 (1982) 460–472.
[21] Solar Fuel GmbH, DE. 10 2009 059 310 A1, 2009.
[22] G.G. Binder, R.R. White, Chem. Eng. Prog. 46 (1950) 563–574.
[23] M. Solc, Collect. Czech. Chem. C. 27 (1962) 2621–2627.
[24] T. Van Herwijnen, H. Van Doesburg, W.A. De Jong, J. Catal. 28 (1973) 391–402.
[25] J.H. Chiang, J.R. Hopper, Ind. Eng. Chem. Prod. Res. Dev. 22 (1983) 225–228.
[26] H. Inoue, M. Funakoshi, J. Chem. Eng. Jpn. 17 (1984) 602–610.
[27] T. Kai, T. Takahashi, S. Furusaki, Can. J. Chem. Eng. 66 (1988) 343–347.
[28] J. Xu, G.F. Froment, AIChE J. 35 (1989) 88–96.
[29] S. Abelló, C. Berrueco, D. Montané, Fuel 113 (2013) 598–609.
[30] L.M. Aparicio, J. Catal. 165 (1997) 262–274.
[31] J. Kopyscinski, T.J. Schildhauer, F. Vogel, S.M.A. Biollaz, A. Wokaun, J. Catal. 271 (2010) 262–279.
[32] J. Kopyscinski, Production of synthetic natural gas in a fluidized bed reactor PhD Thesis, ETH, Zurich, 2010.
[33] J.L. Falconer, A.E. Zağli, J. Catal. 62 (1980) 280–285.
[34] V.M. Shinde, G. Madras, AIChE J. 60 (2014) 1027–1035.
[35] M. Andersson, F. Abild-Pedersen, I. Remediakis, T. Bligaard, G. Jones, J. Engbæk, O. Lytken, S. Horch, J.H. Nielsen, J. Sehested, J. Catal. 255 (2008) 6–19.
[36] D.W. Blaylock, T. Ogura, W.H. Green, G.J. Beran, J. Phys. Chem. C 113 (2009) 4898–4908.
[37] C. Schild, A. Wokaun, R.A. Koeppel, A. Baiker, J. Phys. Chem. 95 (1991) 6341–6346.
[38] P. Bothra, G. Periyasamy, S.K. Pati, Phys. Chem. Chem. Phys. 15 (2013) 5701–5706.
[39] E. Vesselli, L. De Rogatis, X. Ding, A. Baraldi, L. Savio, L. Vattuone, M. Rocca, P. Fornasiero, M. Peressi, A. Baldereschi, R. Rosei, G. Comelli, J. Am. Chem. Soc. 130 (2008) 11417–11422.
[40] G. Peng, S. Sibener, G.C. Schatz, S.T. Ceyer, M. Mavrikakis, J. Phys. Chem. C 116 (2012) 3001–3006.
[41] F.J. Dumez, L.H. Hosten, G.F. Froment, Ind. Eng. Chem. Fund. 16 (1977) 298–301.
[42] G.H. Jonker, J.-W. Veldsink, A.A. Beenackers, Ind. Eng. Chem. Res. 36 (1997) 1567–1579.
[43] Y.-x. Pan, C.-j. Liu, Q. Ge, J. Catal. 272 (2010) 227–234.
[44] A.E. Aksoylu, A.N. Akin, Z.İ. Önsan, D.L. Trimm, Appl. Cat. A 145 (1996) 185–193.
[45] P. Panagiotopoulou, D.I. Kondarides, X.E. Verykios, Appl. Cat. B 88 (2009) 470–478.
[46] T. Inui, M. Funabiki, Chem. Lett. 7 (1978) 251–252.
[47] R. Maatman, S. Hiemstra, J. Catal. 62 (1980) 349–356.
[48] D.E. Peebles, D.W. Goodman, J.M. White, J. Phys. Chem. 87 (1983) 4378–4387.
[49] D. Schlereth, O. Hinrichsen, Chem. Eng. Res. Des. 92 (2014) 702–712.
[50] M. Peter, M.B. Fichtl, H. Ruland, S. Kaluza, M. Muhler, O. Hinrichsen, Chem. Eng. J. 203 (2012) 480–491.
[51] D. Chen, R. Lødeng, H. Svendsen, A. Holmen, Ind. Eng. Chem. Res. 50 (2010) 2600–2612.
[52] L. Maier, B. Schädel, K. Herrera Delgado, S. Tischer, O. Deutschmann, Top. Catal. 54 (2011) 845–858.
[53] M. Kleiber, R. Joh, VDI-Wärmeatlas, Springer Berlin Heidelberg, 2006, pp. 103–132.
[54] N. Wakao, S. Kaguei, T. Funazkri, Chem. Eng. Sci. 34 (1979) 325–336.
[55] P.B. Weisz, C.D. Prater, Adv. Catal. 6 (1954) 142–196.
[56] J.B. Anderson, Chem. Eng. Sci. 18 (1963) 147–148.
[57] D.E. Mears, Ind. Eng. Chem. Proc. Des. Dev. 10 (1971) 541–547.
[58] A.F. Holleman, E. Wiberg, N. Wiberg, Lehrbuch der Anorganischen Chemie, 102 ed., Walter de Gruyter, Berlin, 2007.
[59] K. Mocala, A. Navrotsky, J. Am. Ceram. Soc. 72 (1989) 826–832.
[60] P.H. De Korte, E. Doesburg, C.P. De Winter, L.L. Van Reijen, Solid State Ionics 16 (1985) 73–80.